DIPARTIMENTO DI MECCANICA

mecc

From pulsed to continuous wave emission in SLM with contemporary fiber laser sources: effect of temporal and spatial pulse overlap in part quality

Demir, ALI GOKHAN; Colombo, Paolo; Previtali, Barbara

From pulsed to continuous wave emission in SLM with contemporary fiber laser sources:

Effect of temporal and spatial pulse overlap in part quality

Ali Gökhan Demir*, aligokhan.demir@polimi.it

Paolo Colombo, paolo.colombo@polimi.it

Barbara Previtali, barbara.previtali@polimi.it

Department of Mechanical Engineering, Politecnico di Milano, Via La Masa 1, 20156 Milan, Italy

*Corresponding author

From pulsed to continuous wave emission in SLM with contemporary fiber laser sources: Effect of temporal and spatial pulse overlap in part quality

Ali Gökhan Demir*, aligokhan.demir@polimi.it

Paolo Colombo, paolo.colombo@polimi.it

Barbara Previtali, barbara.previtali@polimi.it

Department of Mechanical Engineering, Politecnico di Milano, Via La Masa 1, 20156 Milan, Italy

*Corresponding author

Abstract

In this work, the effect of pulse temporal and spatial overlapping is evaluated in selective laser melting (SLM). An SLM system operating with fiber laser in pulsed wave (PW) emission was employed. The test material was 18Ni300 maraging steel, which shows reduced process stability due to a high amount of vapour and spark generation during the process. The pulsation characteristics of contemporary power modulated fiber lasers compared to previously employed Q-switched Nd:YAG systems are explained. Processing conditions are studied moving towards continuous wave (CW) by increasing the duty cycle with fixed fluence. The key quality aspects, namely part density and dimensional error, were evaluated and the robustness was assessed. The results demonstrate that with a limited amount of increase in duty cycle by 3%, part density can be improved, while the dimensional error increases. The results show that CW is preferable when fully dense large parts have to be obtained. On the other hand, operating in PW is convenient when thin struts as in lattice structure or micro and precise features are required.

1. Introduction

After more than two decades of process and system development, selective laser melting (SLM) has reached industrial reality. Several machine manufacturers produce fully automated systems capable handling large amounts of metallic powder (up to 100 kg) and processing them to realize parts with different build heights (0.1-0.5 m). While the main system concept remains the same, these systems differ mainly in powder

deposition, gas handling and laser scan strategies employed. Among these, the laser scan strategy is a key factor regarding the part quality indicators, namely porosity, surface roughness, dimensional accuracy and mechanical properties. The usual choice of the industrial system for SLM is a single mode fibre laser (Yb:glass) due to the high brilliance and good absorptivity of most materials to 1 µm radiation. Fiber lasers have become an enabling tool for the SLM process also due to high stability in prolonged use and ease of control owing to their simpler opto-electronic architecture. In the industrial systems, an important primary distinction can be made in terms of the emission mode employed. A greater part of the industrial systems employs continuous wave (CW) emission [1-5]. Other systems use pulsed emission (PW) by power modulation of the fiber laser [3,6]. Such pulsed emission is achieved modulating the laser emission by fast switching of electrical current injected to the pumping diodes. Thanks to the fast responsivity of the fiber laser, pulse durations in µs regime can easily be achieved with kHz level pulse repetition rates.

There is no clear consensus over the use of CW or PW within the SLM process. In scientific literature, a few works compare the CW and PW emissions with older Nd:YAG systems [22,39]. However, these systems are characterized by lower brilliance (bigger spot), and their pulsation mechanism is remarkably different from contemporary fiber lasers. In the case of Nd:YAG lasers, PW is employed mainly to achieve high peak powers in order to overcome the drawback of the large spot, which decreases energy density. These pioneering works often report reduced part densities (<96%), which is overcome by today's industrial SLM systems. On the other hand, industrial SLM systems are facing more stringent requirements for part quality from the sectors they serve, especially aerospace and biomedical, but also automotive, design and tool making. Porosity even at low levels (<2%) can be problematic for fatigue properties. There is an increasing demand for achieving near net-shape products with SLM, avoiding post-processing steps for improving geometrical tolerances, surface roughness and mechanical properties. Compared to CW, PW emission can provide a more flexible control over the heat input by controlling the pulse overlap in scan direction and between the adjacent scan lines. Hence, PW can be highly beneficial for small components and lattice structures, which are sensitive to heat input. PW emission can also improve geometrical integrity due to a more accurate positioning of each pulse position on the scanned area compared to raster lines. On the other hand, PW can intrinsically introduce melt pool instability due to the intermittent process, as observed in laser welding [7]. To date, there are no

works investigating the differences between PW and CW emissions concerning the use of power modulated fiber lasers.

Accordingly, this work provides a basis for a comparison between different emission strategies in SLM. First of all, the literature on the use of different PW systems in SLM is analysed to provide the main concepts. In the experimental section, an SLM system operating with a PW fiber laser was used to study 18Ni300 maraging steel powder. The aim was to reveal whether pulse temporal or spatial overlap can improve the part quality in terms of density and dimensional error with fixed fluence. Particularly, SLM parameter combinations were regulated to move from pulsed to continuous regime, maintaining the amount of energy deposited over the area. Design of experiments was employed to reveal the statistical significance of exposure time and pulse overlap at fixed fluence. The results show that with fixed fluence, density can be improved even with a limited amount of increase in duty cycle. On the other hand, dimensional accuracy is reduced moving towards CW conditions.

2. Use of PW emission in SLM

Some basic concepts regarding PW emission should be defined for a better understanding of the processing conditions. In particular the pulse shape and duration determine the release of energy onto the processed material [8,37,38]. In SLM applications, the pulsation mechanism can vary mainly between Q-switching and power switching of free-running lasers. Q-switching is commonly used with Nd:YAG lasers, where the pulse shape and duration is determined by the laser cavity and Q-switching method. The method commonly generates high peak powers in kW range with relatively low average power and pulse repetition rates. Fiber lasers, on the other hand, allow for a fast modulation through their integrated opto-electronic design. Owing to the fast power modulation of pump diodes, the laser can be pulsated. In this case, the produced pulses are commonly in a square wave shape and the peak power is the same as the power level obtainable at CW mode. The temporal behaviour of the pulse wave emission is represented in Figure 1.a. Regardless of the pulsation mode, the pulse energy (E) can be calculated as:

$$E = \int_0^{t_{on}} P(t)dt \qquad\qquad\qquad Eq.(1)$$

where $P(t)$ is the power level which can vary as a function of time t, and t_{on} is the duration of the pulse. Pulse repetition rate (PRR) can be defined as:

$$PRR = \frac{1}{t_{on}+t_{off}}$$
Eq.(2)

where t_{off} is the temporal distance between the end of the pulse and the beginning of the consecutive one. Hence, average power (P_{avg}) in PW emission can be calculated as:

$$P_{avg} = E \cdot PRR$$
Eq.(3)

Another important factor that determines the PW emission characteristics is the duty cycle (δ), which expresses the laser on time over the whole pulsation period and can be calculated as:

$$\delta = \frac{t_{on}}{t_{on}+t_{off}}$$
Eq.(4)

The increasing duty cycle moves the emission regime towards CW, where 100% duty cycle corresponds to CW emission. For square-wave shaped pulses, the pulse profile does not vary throughout the pulse duration. Hence, the average power can be calculated as:

$$P_{avg} = \frac{P_{peak} \cdot t_{on}}{t_{on}+t_{off}} = P_{peak} \cdot \delta$$
Eq.(5)

where P_{peak} is the peak power of the pulse. While the previous parameters express the PW emission characteristics in time, pulse overlap (O_p) in space is another key factor, governed by point distance (d_p) parameter (see Figure 1.b). For a given laser beam diameter (d_s), if each pulse is placed with a certain point distance (d_p), pulse overlap can be calculated as:

$$O_p = (d_s - d_p)/d_s$$
Eq.(6)

For a stationary beam pulse overlap is 100%, which reduces by the increase of point distance. On the other hand, line overlap (O_l) between consecutive scan lines depends on hatch distance (d_h) and can be calculated as:

$$O_l = (d_s - d_h)/d_s$$
Eq.(7)

5

For a beam passing over the same line, line overlap is 100%. Both pulse and line overlap can be negative, if point distance or hatch distance is larger than the beam diameter. It should be noted that molten pool can be larger than the laser beam diameter, hence even with negative pulse or line overlaps continuous molten tracks can be achieved.
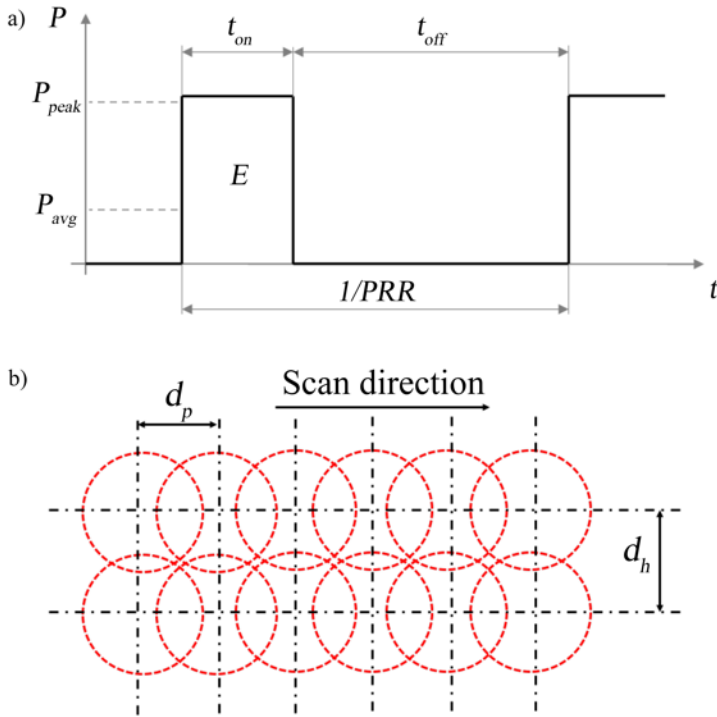
Figure 1. Schematic representation of a) temporal and b) spatial disposition of pulses.

Literature survey shows that PW emission is explored relatively less compared to CW in SLM. The use of the keyword "selective laser melting" in the Web of Knowledge database produces 1966 results referring to publications between 1997 and 2016 (last access on 28 June 2016). On the other hand, through a detailed analysis, 69 articles were found reporting the use PW emission in SLM. The main characteristics of the used laser systems, along with the used material and maximum relative density (ρ_{max}) achieved in the studies are reported in Appendix A (see Table A. 1). Pulse characteristics (t_{on}, PRR, P_{avg}, P_{peak}, δ) are reported in a representative range for each work. If data were not explicitly provided, they were calculated using the available information, where applicable. Figure 2 summarizes the main results of the analysis. It can be observed that a certain technological change occurred around 2010 with the industrial implementation of fiber lasers in SLM systems (see Figure 2). Until that period, Q-switched Nd:YAG lasers were employed extensively

6

integrated to in-house developed systems carrying out the pioneering works in SLM. Nd:YAG lasers improved absorptivity in metals compared to CO_2 counterparts. However, the large beams - due to the low beam quality - had to be compensated by high peak powers. Pulse durations were mainly in ms region, whereas ns pulses were also employed. The resultant duty cycles were low, in some cases <1%. At a proof-of concept stage, part densification was studied on single track geometries or complete parts were not producible. In the later period, parts were produced commonly with low density (<96%), due to the low beam brilliance and reduced duty cycles. The use of Q-switched Nd:YAG lasers with ns pulses has also been preferred specifically for micro parts, despite the low densities achieved [34].

The introduction of fiber lasers provided high brilliance beams with a smaller diameter. With the ease of integration and robustness provided by these lasers, different system producers developed industrial grade SLM systems. The beam brilliance allowed to operate at CW emission, without the need for high peak powers to melt material, owing to which many system producers took up this strategy. PW emission has also been employed in order to provide higher flexibility in process parameters, which can be beneficial for managing the heat input. It is no surprise that in literature all the SLM systems integrating PW fiber lasers are industrial machines. The literature review shows that with the introduction of PW fiber lasers, the research focus was also shifted to materials such as Ti and Al-alloys, Co-Cr-Mo and W for high-end aerospace, biomedical and automotive applications. These materials for the given applications should be free of defect and are demanding for SLM process due to the high melting temperature, low absorptivity or thermal distortions. Also due to the overall high quality of the produced parts, research themes moved towards finishing operations [67] or advanced applications of the produced components [51,77].

On the other hand, the clear distinction between the differences and advantages of using PW or CW modes with fiber lasers has not been studied. While the overall performance of PW and CW pulsed emissions with fiber lasers is beyond the performance of their ancestors, Nd:YAG lasers, in certain applications the distinction between the two emission regimes becomes more relevant. In particular, materials with a high melting point [56], reflective materials [76], fine geometries and materials prone to spark and vapour generation can require different emission modes in order to ensure full density, low roughness and low thermal distortion. For high-end applications part density is expected to be higher than 99%, in order to maintain the required mechanical

strength both in static and dynamic conditions. As seen in the literature review, high part density is not readily achievable with PW fiber lasers for all materials and a study of process parameters is required (see Table A. 1). Maraging steel, from this point of view, shows difficulty in maintaining high density over large components. The use of a correct processing strategy is a critical point for increased robustness. Therefore, the effect of moving from PW towards CW emission by controlling temporal and spatial pulse overlap is highly important. Previous works on 18Ni300 maraging steel have been carried out with CW emission [78-81]. Yasa et al. [78] reported relative density around 99%, whereas Casalino et al. [81] reported density higher than 99%.

Another recent development is the use of ultrafast pulses in SLM as presented by Bai et al [68,71]. The authors propose a bonding mechanism based on ionization with the use of ps- to fs-long pulses. In this regime the authors demonstrate that very small details can be achieved on parts and microstructural manipulation is possible.
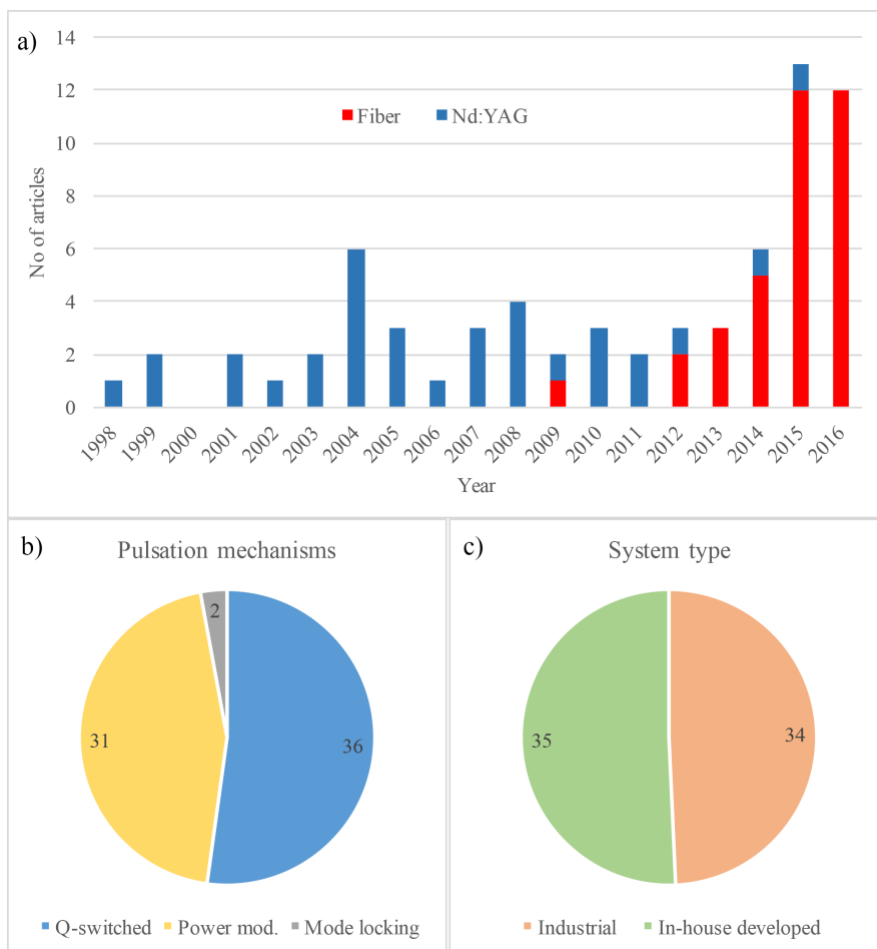
Figure 2. Main results of the literature survey on the use of PW in SLM. a) Number of articles published per year. Distribution of different b) pulsation mechanisms and c) system types used.

3. Experimental

3.1. SLM system

Renishaw AM250 was used throughout the experimental work (Stone, UK). The system implemented a 200 W active fiber laser (R4 from SPI, Southampton, UK). The optical chain was composed of a galvanometric scanner with integrated z-axis positioner, which enabled to control the focal position of the beam. In this configuration the estimated beam diameter is 75 μm. The build space was 250x250x300 mm3 (WxDxH). Prior to processing, vacuum is applied to the processing chamber down to -950 mbar pressure and then it is flooded with Ar reaching 15 mbar overpressure. Throughout the process, a circulation pump maintains the gas flow parallel to the powder bed and the oxygen content of the process chamber is maintained below 1000 ppm.

The system employed the PW emission. In particular, the laser is positioned on a certain spot to emit with a given peak power (P_{peak}) for a fixed exposure time (t_{on}) in μs range. The laser jumps onto the consecutive spot on the scanned line and applies the exposure. At the end of each scanned line, the laser jumps to the adjacent one. The operation is continued until the layer is scanned completely. For a given layer, the system applies different hatch lines for the part volume and part external border, which use different parameter sets (see Figure 3.a). Beam compensation can be applied by placing the external border inward with respect to the design geometry defined by the STL border.

Five principal process parameters have been identified for the study. The laser power controls the pulse peak power (P_{peak}). Pulses are generated by power modulation with a shape very close to a square wave. Hence, the emission profile does not vary throughout the pulse duration, *i.e. P(t)=P_{peak}*. Exposure time controls the duration of the laser pulse applied to each spot on the scanned line and corresponds to t_{on}. The minimum exposure time that can be employed is 20 μs. The focal position (*f*) controls the position of the beam focal point with respect to the powder bed surface. For the present system, negative focal position values refer to a laser spot focused above the powder bed surface, and positive values refer to the focal point below the powder bed surface (see Figure 3.b). The focal position controls the spot size (d_s) on the powder surface and in either case the beam size enlarges moving away from the focal position. Point distance (d_p) and hatch distance (d_h) are the other parameters that were varied.

For support generation, slicing and post processing of the layer trajectories Magics 19 was used (Materialise, Leuven, Belgium).
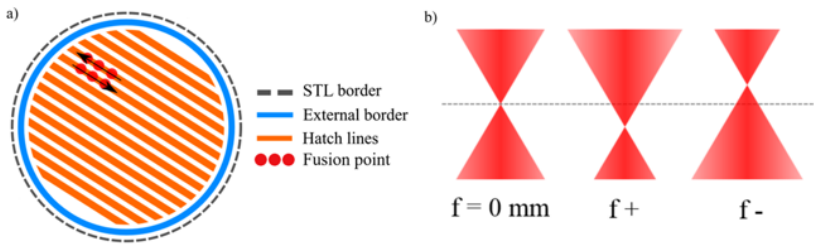
Figure 3. a) Positioning of STL border with respect to the scanned external border and hatch lines composed of different fusion points. b) Change of beam size as function of focal position f.

3.2. Material

Throughout the study 18Ni300 maraging steel powder was used (Sandvik Osprey, Neath, UK). The powder was atomized in nitrogen and characterized by a spherical shape. The average particle size was 32 μm and with 5 g/cm$_3$ tap density. The nominal material density is 8.1 g/cm$_3$ [78]. Nominal chemical composition and particle size distribution are reported in Table 1 and Figure 4 respectively.

Table 1. Chemical composition of the maraging steel 18Ni300 powder declared by the producer.

Element	Ni	Co	Mo	Ti	Cr	Si	Mn	Al	Cu
wt%	17.6	9.6	5.3	0.7	0.49	0.1	0.1	0.09	0.05

Figure 4. Size distribution and SEM image of the 18Ni300 maraging steel powder.

3.3. Characterization equipment

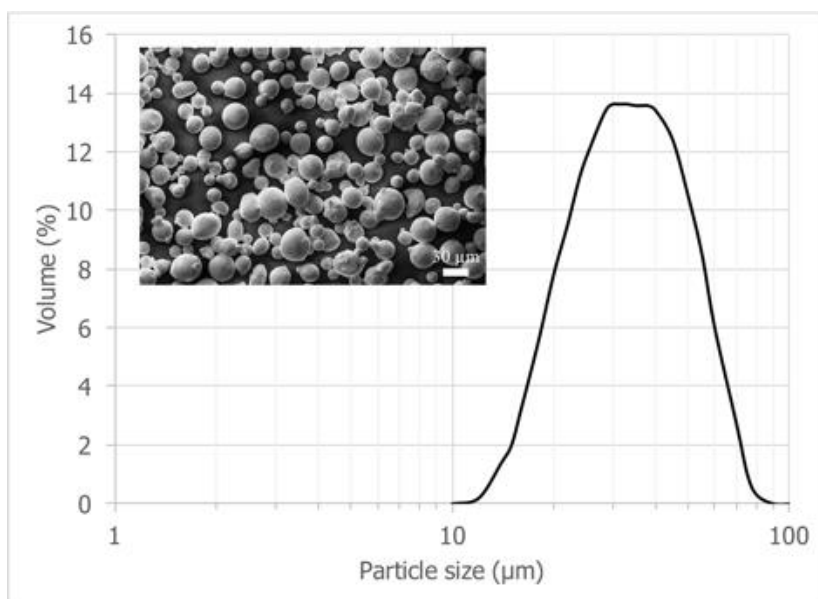Part density was measured using Archimedes method. Each built part was weighted in air and in pure water using a high precision balance with a dedicated measurement kit (Precisa 100A-300M, Turin, Italy). Metallographic cross-sections of the realized samples were prepared by cutting, mounting in resin and polishing. Optical microscopy images of the cross sections were acquired with 5X magnification (Quick Vision ELF from Mitutoyo, Kawasaki, Japan). Scanning electron microscope was also used to examine cross-sections (SEM, EVO-50 from Carl Zeiss, Oberkochen, Germany). Dimensional accuracy of the build parts was assessed using a coordinate measurement machine (CMM, Prismo 5 VAST MPS HTG from Carl Zeiss, Oberkochen, Germany).

3.4. Moving towards CW emission with fixed fluence

In order to assess the effects of temporal and spatial pulse overlap, the experiments were carried out with fixed energy density, namely fluence, which is defined by the following equation.

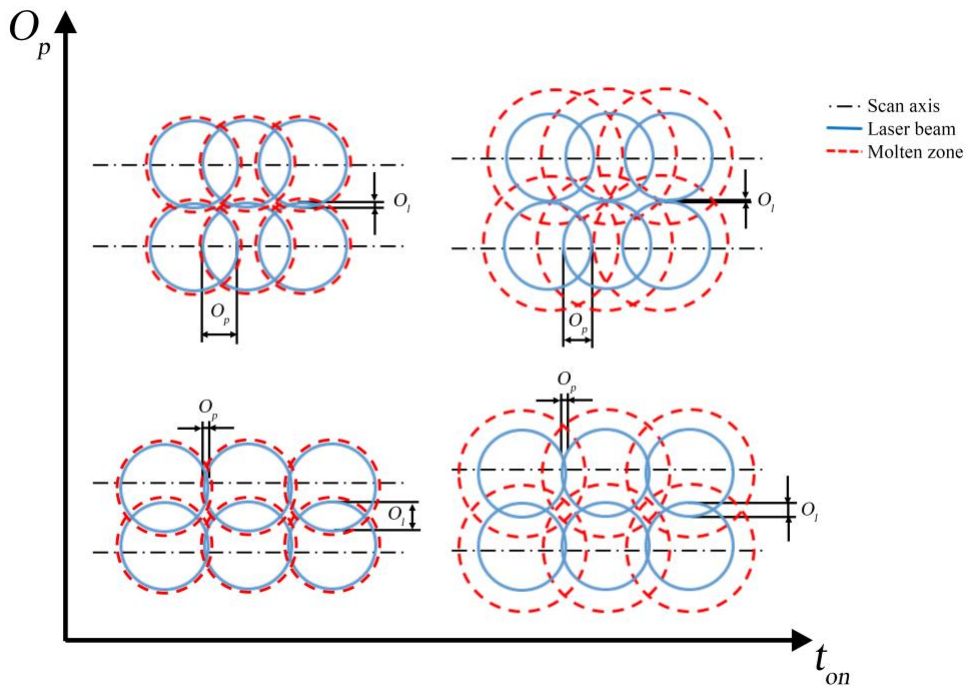$$F = \frac{P_{peak} \cdot t_{on}}{d_p \cdot d_h}$$

Eq.(8)

Figure 5. Schematic representation of pulse positions within a scan line and between adjacent scan lines.

For fixed fluence, the effect of varying exposure time (t_{on}) and pulse overlap (O_p) is schematically shown in Figure 5. The influence of increased exposure time is represented by an increase of the molten zone diameter. The same effect can be expressed mathematically by rewriting Eq.6 substituting d_p and d_h.

$$F = \frac{P_{peak} \cdot t_{on}}{(d_s - O_p \cdot d_s) \cdot (d_s - O_l \cdot d_s)} \qquad \text{Eq.(9)}$$

From Eq.(9), it can be seen that in order to keep fluence constant, for fixed pulse overlap (O_p), the increase of exposure time (t_{on}) should be compensated by lowering the line overlap (O_l). Therefore, the adjacent lines move closer to each other.

On the other hand, with fixed exposure time, if the pulse overlap increases (O_p), then the line overlap (O_l) should be reduced to maintain the fluence. As a consequence, the adjacent lines move away from each other.

3.5. Experimental design and test geometries

A parameter set recommended by the system producer was used as reference condition (P_{peak}=200 W, t_{on}=80 μs, d_p=65 μm, d_h=80 μm, f=0 mm), which produced 308 J/cm^2 fluence. The focal position was fixed at powder bed surface (f=0 mm), employing the smallest spot size. The laser peak power was fixed at the highest value (P_{peak}=200 W). Layer thickness (z) of 40 μm was used throughout the experiments. In this specific case the t_{off} can be calculated as:

$$t_{off} = d_p / v_s \qquad \text{Eq.(10)}$$

where, v_s is the average scan speed between consecutive laser spots, equal to 5 m/s. In the experimental plan, fluence was fixed to the level obtained with the recommended parameter set, and conditions were varied to move closer to CW emission. The employed experimental design was 2_2 full factorial plan with exposure time (t_{on}) and pulse overlap (O_p) as the varied parameters. The experimental plan is summarized in Table 2. For each level of exposure time, high and low pulse overlap levels were determined by varying the point distance. Hatch distance was calculated using Eq. (8) to maintain the fluence value. The resultant conditions are listed in

Table 3.

Two specific test geometries, namely prism and tower, were employed. Figure 6 shows the dimensions of each geometry as well as photographs of the built parts. Prism geometry is a simple square prism with 15x15 mm$_2$ base and 26 mm height. Prism was used to determine the part density as a function of process parameters. Four parts were produced for each combination. Tower geometry was used for characterizing geometrical error. It was composed of a square prism base (20x20x6 mm$_3$) and an extruded section (10x10x20 mm$_3$). Dimensions of the extruded section were measured and the average dimensional error was calculated using the following expression

$$e_{avg} = \frac{l_{m,x}+l_{m,y}}{2} - l_n \qquad \qquad \text{Eq.(11)}$$

where $l_{m,x}$ and $l_{m,y}$ are the measured length on x and y axes respectively, and l_n is the nominal length of the part described by the STL file. Two parts were produced for each parameter combination. The density of the tower specimens was also measured.
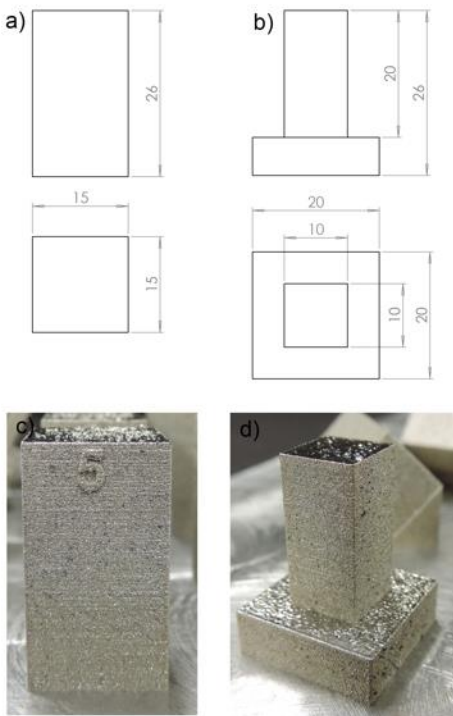
Figure 6. Technical drawings of the test geometries (a,b) and photographs of the produced parts (c,d). Prism for density study (a,c) and tower for dimensional error characterization (b,d)

13

All specimens were produced also using the process parameter combinations recommended by the SLM system producer for comparison purposes. The analysis of variance was applied to determine the effects of process parameters on the response variables. The statistical significance level was set as α=5%. Residuals were controlled for normality and homogeneity.

In all the experimented conditions, a single external border was applied. The laser parameters employed for the external border were recommended by the system producer (P=150 W, t_{on}=50 µs, d_p=20 µm, f=0 mm) and kept constant throughout the experimentation.

Table 2. Fixed and varied parameters as function of test geometries and response variables

Fixed parameters	
Laser peak power, P_{peak} (W)	200
Focal position, f (mm)	0
Layer thickness, z (µm)	40
Varied parameters	
Exposure time, t_{on} (µs)	70, 90
Pulse overlap, O_p	Low, High
Measured variables	
Part density, ρ (%)	
Average dimensional error, e_{avg} (µm)	

Table 3. Process parameter combinations tested in the study with corresponding pulse temporal and spatial characteristics.

| Strategy	t_{on}(µs)	d_p (µm)	d_h (µm)	O_p	O_l	t_{off} (µs)	δ	P_{avg} (W)
t_{on}=80 µs Med O_p - Recommended	80	65	80	13%	-7%	13	86.0%	172.0
t_{on}=70 µs, Low O_p	70	65	70	13%	7%	13	84.3%	168.6
t_{on}=70 µs, High O_p	70	57	80	24%	-7%	11	86.0%	172.0
t_{on}=90 µs, Low O_p	90	73	80	3%	-7%	15	86.0%	172.0
t_{on}=90 µs, High O_p	90	65	90	13%	-20%	13	87.4%	174.8

4. Results

4.1. Part density

Part density varied between 7.773 and 7.996 g/cm3 in the experimented combinations, corresponding to 96.0-98.7% of the nominal density of the material. As shown in Table 4, exposure time is the only effective parameter in varying the part density, as both pulse overlap and interaction were not significant. Figure 7.a shows the main effects plot for the density of the prims parts. In particular, a higher exposure time with fixed fluence improves the part density.

Table 4. ANOVA table for density (ρ (%)).

Source	DF	Adj SS	Adj MS	F-Value	P-Value
t_{on} (μs)	1	0.000323	0.000323	10.15	0.008
O_p	1	0.000079	0.000079	2.49	0.140
t (μs)·O_p	1	0.000016	0.000016	0.51	0.488
Error	12	0.000382	0.000032		
Total	15	0.000800			
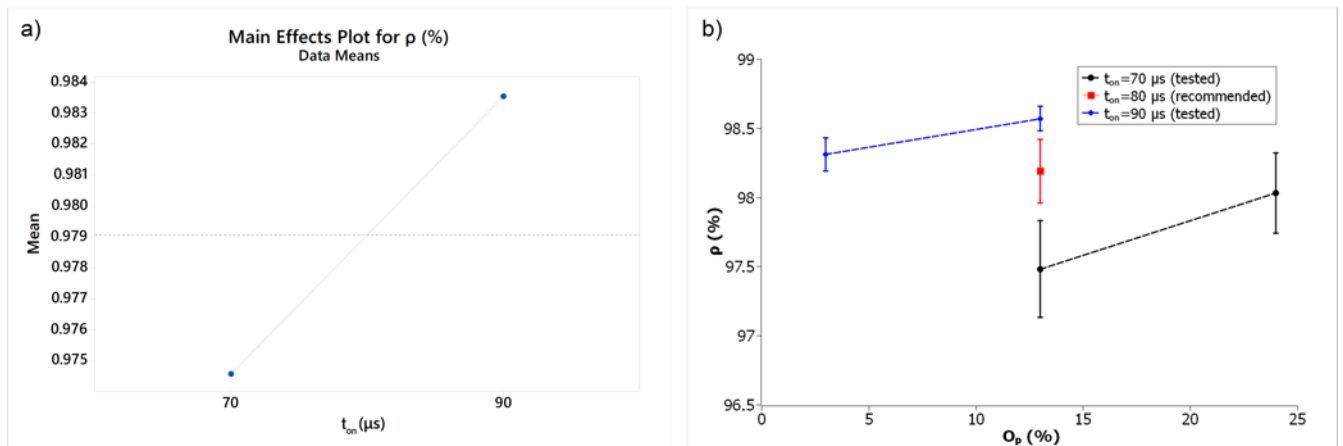
Figure 7. a) Main effects plots part density showing the effect of the statistically significant parameter exposure time (t_{on}). b) Density comparison between different processing strategies (error bars represent standard error).

Figure 7.b shows the density variation for each strategy. The density measurements of tower samples are pooled in this graph. It can be seen that with increased exposure time and pulse overlap, at fixed fluence conditions the part density increases. As shown in Figure 7.b, the highest group average and smallest standard error interval corresponds to the highest average power condition (t_{on}=90 μs, O_p=13%, P_{avg}=174.8 W). For this condition, the average density lies over 98.5%. The lowest average and the highest standard error are achieved

with the same pulse overlap, but with reduced average power (t_{on}=70 μs, O_p=13%, P_{avg}=168.4 W) strengthening the importance of temporal pulse overlap over spatial component. In this configuration, the process strategy shows variability of part density between 97% to above 98%. It can also be seen that the recommended condition by the system manufacturer falls between the experimented conditions within the factorial plan, following the general trend. Figure 8 shows the cross section images of conditions with lowest and highest density. It can be seen that the use of low temporal pulse overlap (t_{on}=70 μs, O_p=13%, P_{avg}=168.4 W) produces large pores dispersed around the part (see Figure 8.a). The close up SEM image shows that the pore is filled with non-molten powder particles (see Figure 8.c). The porosity is lower in amount (see Figure 8.b) and smaller in size (see Figure 8.d) with increased temporal pulse overlap (t_{on}=90 μs, O_p=13%, P_{avg}=174.8 W).
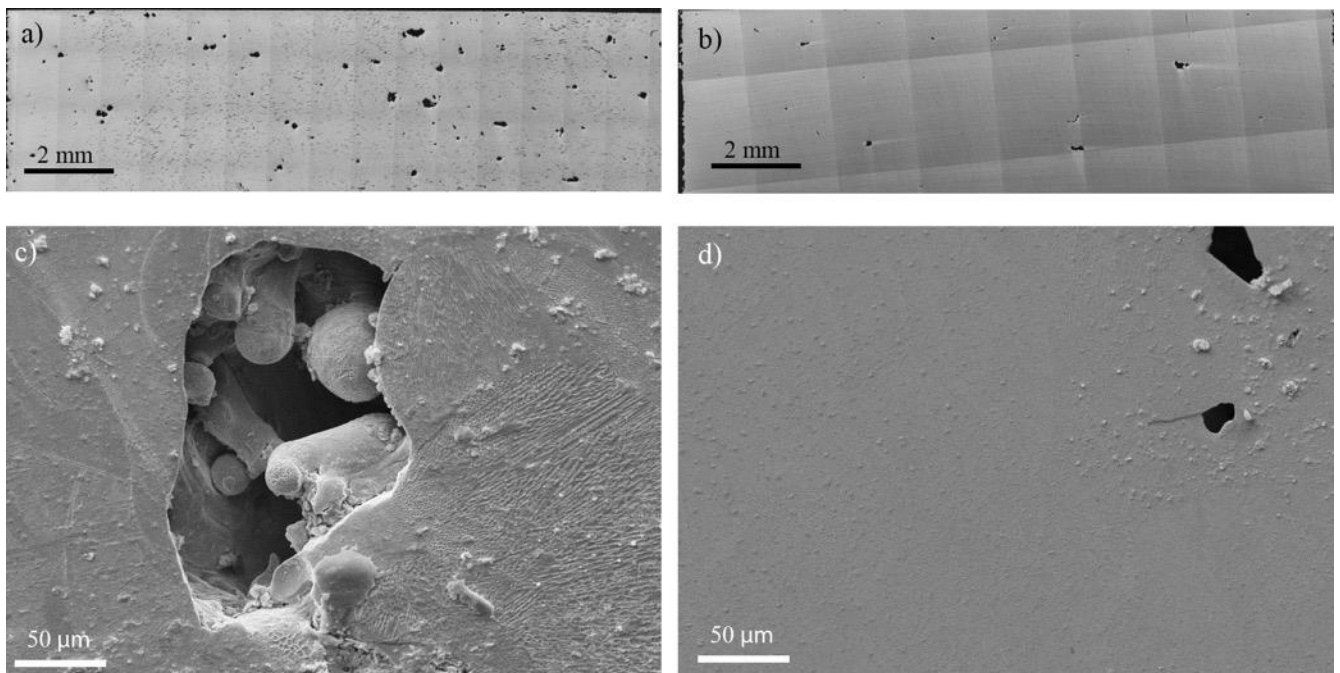
Figure 8. Optical microscopy and SEM images of the sample cross sections showing pore morphology. Highest (a,c) porosity obtained with t_{on}=70 μs and O_p=13% (P_{avg}=168.4 W); and lowest porosity conditions (b,d) obtained with t_{on}=90 μs and O_p=13% (P_{avg}=174.8 W).

4.2. Dimensional error

The measured dimensional error varied between 363 and 454 μm. In terms of statistical significance, exposure time (t_{on}) was found to vary the dimensional error (see Table 5). The main effects plot of the only statistically significant parameter, exposure time, is reported in Figure 9.a. The influence of exposure time on the dimensional error can be attributed to the expansion of the molten and solidified area. Despite the fact that

border line is applied with fixed conditions, the extent of molten and solidified material also depends on the scan parameters of the volume.

Figure 9.b compares the different processing strategies with the recommended one. It can be seen that the geometrical error increases following a similar trend to the density increase. Also in this case the recommended condition by the system manufacturer falls between the experimented conditions within the factorial plan, following the general trend. Moving away from CW emission appears to be more beneficial for maintaining the dimensional accuracy.

It can be expected that the dimensional error measured is close to the molten track width, which varies with process parameters. Following the same trend with density measurements, the dimensional error indicates that an increase of t_{on} from 70 to 90 µs is expected to increase the average molten pool size by approximately 125 µm.
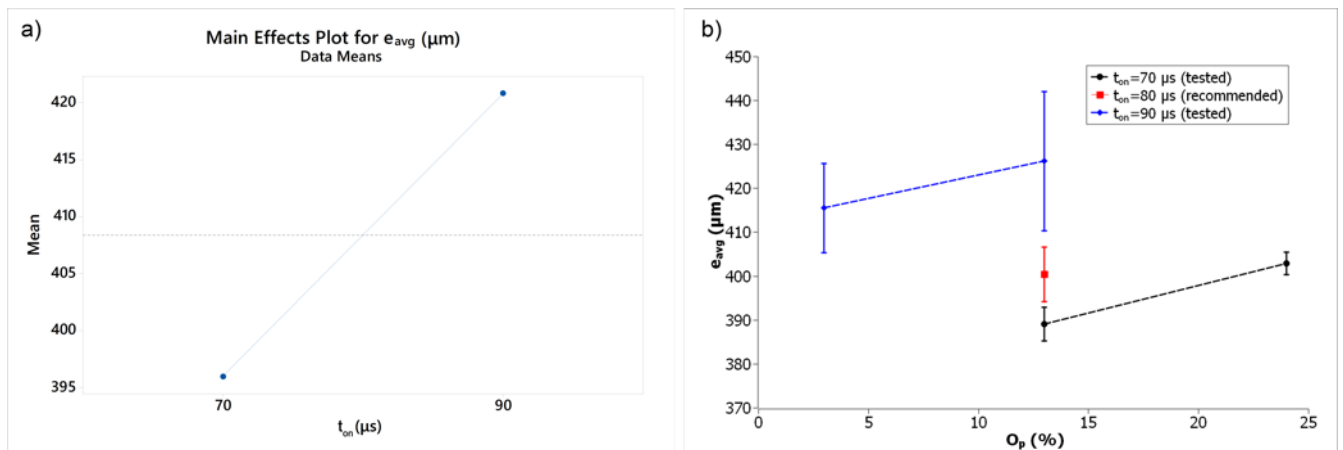
Figure 9. a) Main effects plot for dimensional error showing the effect of the statistically significant parameter exposure time (t). b) Dimensional error comparison between different processing strategies (error bars represent standard error).

Table 5. ANOVA table for average dimensional error (e_{avg}).

Source	DF	Adj SS	Adj MS	F-Value	P-Value
t_{on} (µs)	1	1234.65	1234.65	8.17	0.035
O_p	1	299.16	299.16	1.98	0.218
Error	5	755.42	151.08		
Lack-of-fit	1	4.77	4.77	0.03	0.881
Pure error	4	750.65	187.66		
Total	7	2289.24			

5. Discussion

The experimental results put into evidence that the temporal pulse overlap plays an important role on the part quality. With fixed fluence, it is shown that higher density can be achieved by increasing the duty cycle (δ). Within the limitations of the control scheme available to the end user, experiments were conducted to move the emission conditions towards CW conditions. Within the experimental range, average power (P_{avg}) was varied only by 6.2 W with fixed fluence (F=308 J/cm2) and fixed peak power (P_{peak}=200 W). Such variation generated a density increase of 1.1% in average. Moreover, the pore morphology and dimensions also change, since smaller pores are observed with increased exposure time. This change is remarkable, since the part density variations around these levels can deteriorate the fatigue behaviour drastically.

On the contrary, moving towards increased duty cycle, hence CW, geometrical precision decreases. It can be expected that increased duty cycle maintains a constant molten pool with increased width. While this fact is beneficial for improving the part density, geometrical integrity is also reduced. The dimensional error can be compensated by changing the border distance. However, in order to obtain fine structures, such as lattice or thin walls, the effect of large molten and solidified tracks as well as high roughness are disadvantageous. Employing PW emission with reduced duty cycle, a greater control over the geometrical precision and thermal load can be achieved, which becomes of greater importance with reduced solid mass overhanging on the non-molten powder.

6. Conclusions

This work presents the influence of spatial and temporal pulse overlap in SLM employing PW emission. The process parameters were set to move closer to CW condition with fixed fluence level. Experimental analysis was carried out on 18Ni300 maraging steel, which shows lower processability with SLM due to high porosity. The main outcomes of the work can be listed as follows:

- PW emission is achieved with Q-switching in older Nd:YAG lasers and with power modulation in contemporary fiber lasers. The previously employed Nd:YAG lasers provide high peak powers with low repetition rates, compensating for the low brilliance due to the low beam quality. Pulse profiles

with the fiber lasers are commonly uniform, peak power levels are lower and repetition rates are higher.

- With fixed fluence level, exposure time plays the major role in improving the part density by increasing the average power. This implies that the temporal overlap is more important than spatial overlap over a scanned line.

- Moving towards CW, process robustness against increases higher density is maintained with smaller process variation. In addition to the reduction of porosity, the pore size is also observed to be smaller.

- Dimensional error can be correlated to the melting capability of the processing parameters. Moving towards CW a constant and wider molten track is expected to be generated. Within the experimented range, an increase of 20 μs in exposure time results in 125 μm of increase in geometrical error, which is expected to be close to the enlargement of the melt pool size. This ensures a higher density with higher dimensional error. Thus, the use of PW emission can be more adequate for finer geometries such as lattice structures and thin walls.

Acknowledgements

Appendix A

Table A. 1. Literature survey on the use of PW emission in SLM. Data collection was terminated on 28 June 2016.

Ref.	Year	System	Source	d_s (μm)	PW method	t_{on}	*PRR*[Hz]	P_{avg} (W)	P_{peak} (W)	δ	Material	ρ_{m}
9	1998	In-house developed	Nd:YAG	50	Q-switched	ns	60000	15	2000	0.1%	AISI 316L	n/a
10	1999	In-house developed	Nd:YAG	800	Q-switched	ms	n/a	n/a	2500	n/a	Pure Cu	n/a
11	1999	In-house developed	Nd:YAG	500	Q-switched	n/a	n/a	20	n/a	n/a	Sn-Cu	n/a
12	2001	In-house developed	Nd:YAG	80	Q-switched	ns	30000	70	11667	0.6%	AISI 316L	n/a
13	2001	In-house developed	Nd:YAG	800	Q-switched	ms	50	50	1000	5.0%	Ni alloy	n/a
14	2002	In-house developed	Nd:YAG	800	Q-switched	ms	50	50	1000	n/a	Commercially pure Ti (GI)	95.0%
15	2003	In-house developed	Nd:YAG	620	Q-switched	n/a	n/a	100	5000	n/a	Low carbon steel	95.5%
16	2003	In-house developed	Nd:YAG	400	Q-switched	μs	1000	15	45000	0.1%	Commercially pure Ti	n/a
17	2004	In-house developed	Nd:YAG	100	Q-switched	ns	60000	80	n/a	0.1%	AISI 316L	85.0%
18	2004	In-house developed	Nd:YAG	n/a	Q-switched	n/a	100000	10	n/a	n/a	W	n/a
19	2004	In-house developed	Nd:YAG	n/a	Q-switched	n/a	50000	10	n/a	n/a	W, Al	n/a
20	2004	In-house developed	Nd:YAG	n/a	Q-switched	ms	40	36	n/a	8.0%	Pure Fe, Fe-0.2-0.4 C	95.0%
21	2004	In-house developed	Nd:YAG	100	Q-switched	ns	5000	2	n/a	0.1%	Commercially pure Ti	n/a
22	2004	In-house developed	Nd:YAG	800	Q-switched	ms	50	300	n/a	32.0%	Fe-alloy	n/a
23	2005	In-house developed	Nd:YAG	n/a	Q-switched	n/a	100000	10	n/a	n/a	AISI 316L, W, Ni-alloy	n/a
24	2005	In-house developed	Nd:YAG	n/a	Q-switched	n/a	100000	10	n/a	n/a	W	n/a
25	2005	In-house developed	Nd:YAG	350	Q-switched	ms	80	15	90	24.0%	Ti	65.0%
26	2006	In-house developed	Nd:YAG	750	Q-switched	ms	50	50	1000	5.0%	Various	92.0%
27	2007	In-house developed	Nd:YAG	800	Q-switched	ms	10	9	n/a	5.0%	Waspaloy-Zr	99.6%
28	2007	In-house developed	Nd:YAG	n/a	Q-switched	n/a	100000	10	n/a	n/a	AISI 316L, W, Ni-alloy, Mo, Cu, Ag	n/a
29	2007	In-house developed	Nd:YAG	n/a	Q-switched	ns	100000	10	n/a	2.0%	AISI 316L, W, Ni-alloy, Mo, Cu, Ag	n/a
30	2008	In-house developed	Nd:YAG	800	Q-switched	ms	10	550	1800	5.0%	Waspaloy	99.7%
31	2008	In-house developed	Nd:YAG	n/a	Q-switched	ns	100000	10	n/a	2.0%	AISI 316L, W, Ni-alloy, Mo, Cu, Ag	90.0%
32	2008	In-house developed	Nd:YAG	n/a	Q-switched	ns	100000	10	n/a	2.0%	Ceramic materials, Mo, Cu	n/a
33	2008	Concept Laser M3	Nd:YAG	53	Q-switched	n/a	n/a	n/a	n/a	n/a	AISI 316 L, TI6Al4V	n/a
34	2009	In-house developed	Fiber	12.5	Q-switched	ns	80000	4	280	1.4%	W, Al	95.0%

35	2009	In-house developed	Nd:YAG	800	Q-switched	ms	10	550	1800	2.5%	Inconel 625	n/a
36	2010	Concept Laser M3	Nd:YAG	53	Q-switched	ns	50000	n/a	n/a	n/a	AISI 1045	n/a
37	2010	In-house developed	Nd:YAG	800	Q-switched	ms	10	100	1800	40.0%	Inconel 625	n/a
38	2010	In-house developed	Nd:YAG	800	Q-switched	ms	10	100	1800	40.0%	Inconel 625	n/a
39	2011	In-house developed	Nd:YAG	600	Q-switched	ns	50000	26	26000	0.1%	Pure Mg	n/a
40	2011	In-house developed	Nd:YAG	600	Q-switched	ns	50000	26	26000	0.1%	Pure Mg	n/a
41	2012	In-house developed	Nd:YAG	150	Q-switched	ns	20000	100	n/a	<2%	AISI 316L, pure Ag	n/a
42	2012	Renishaw AM 250	Fiber	70	Power mod.	µs	4348	191	200	95.7%	Ti6Al4V	n/a
43	2012	Renishaw AM 250	Fiber	n/a	Power mod.	µs	n/a	200	n/a	n/a	Ti6Al4V	n/a
44	2013	In-house developed	Fiber	12.5	Q-switched	ns	80000	4	280	1.4%	Molybdenum	n/a
45	2013	Renishaw AM 25	Fiber	70	Power mod.	µs	9091	200	220	90.9%	H20	97.5%
46	2013	Renishaw AM 125	Fiber	70	Power mod.	µs	n/a	n/a	200	n/a	AISI 316L	n/a
47	2014	Renishaw AM250	Fiber	70	Power mod.	µs	n/a	n/a	200	n/a	Ti6Al4V	n/a
48	2014	MTT 250	Fiber	n/a	Power mod.	µs	3831	192	200	96.2%	Ti6Al4V	n/a
49	2014	Renishaw AM 250	Fiber	n/a	Power mod.	µs	4348	200	209	95.7%	Ti6Al4V	n/a
50	2014	In-house developed	Nd:YAG	25	Q-switched	ns	n/a	500	8300	n/a	Molybdenum	n/a
51	2014	Renishaw SLM 125	Fiber	70	Power mod.	µs	8929	179	200	89.3%	AISI 316L	n/a
52	2014	Renishaw AM 250	Fiber	70	Power mod.	µs	4348	191	200	95.7%	Ti6Al4V	n/a
53	2015	Renishaw AM 250	Fiber	75	Power mod.	µs	8772	200	228	87.7%	Co-Cr-Mo	>99%
54	2015	In-house developed	Nd:YAG	150	Q-switched	ms	n/a	n/a	4500	n/a	Al12Si	95.0%
55	2015	Renishaw SLM 125	Fiber	70	Power mod.	µs	n/a	n/a	n/a	n/a	AlSi12	n/a
56	2015	Renishaw AM 250	Fiber	75	Power mod.	µs	3226	194	200	96.8%	Tungsten	n/a
57	2015	Renishaw AM 250	Fiber	70	Power mod.	µs	14285	200	264.16	75.7%	Aisi 304L	n/a
58	2015	Renishaw AM 250	Fiber	70	Power mod.	µs	9091	182	200	90.9%	AISI 316L	99.6%
59	2015	Renishaw AM 250	FIber	n/a	Power mod.	µs	6410	200	223	89.7%	AlSi10Mg	n/a
60	2015	Renishaw AM 250	Fiber	n/a	Power mod.	µs	n/a	200	n/a	n/a	Ti6Al4V	97.6%
61	2015	Renishaw AM 250	Fiber	70	Power mod.	µs	n/a	n/a	200	n/a	AlSi10Mg	n/a
62	2015	Renishaw SLM 125	Fiber	70	Power mod.	µs	6250	169	180	93.8%	Hastelloy X	>99%
63	2015	Renishaw AM 250	Fiber	n/a	Power mod.	µs	n/a	400	n/a	n/a	Duplex SS	<90%
64	2015	Renishaw AM 250	Fiber	75	Power mod.	µs	6061	200	220	90.9%	Ti6Al4V	n/a

65	2015	Renishaw AM 250	FIber	75	Power mod.	µs	8772	200	228	87.7%	Co-Cr-Mo	n/a
66	2016	Renishaw AM 250	Fiber	70	Power mod.	µs	13333	100	125	80.0%	Ti6Al4V	94.6%
67	2016	Renishaw SLM 125	Fiber	35	Power mod.	µs	n/a	n/a	n/a	n/a	AISI 316L	n/a
68	2016	In-house developed	Fiber	n/a	Mode locking	fs	10_8	1000	n/a	10_{-7}	W	>99.%
69	2016	Renishaw AM 250	FIber	70	Power mod.	µs	n/a	200	n/a	n/a	AlSi10Mg	n/a
70	2016	Renishaw AM 250	Fiber	75	Power mod.	µs	n/a	200	n/a	n/a	AISI 316L	99.8%
71	2016	In-house developed	Fiber	n/a	Mode locking	fs	n/a	n/a	n/a	n/a	W	n/a
72	2016	Renishaw AM 250	FIber	n/a	Power mod.	µs	10000	200	222	90.0%	AISI 316L	n/a
73	2016	Renishaw AM 250	Fiber	70	Power mod.	µs	n/a	n/a	n/a	n/a	n/a	n/a
74	2016	Renishaw AM 250	Fiber	70	Power mod.	µs	n/a	190	n/a	n/a	Ti6Al4V	99.0%
75	2016	Renishaw AM 250	Fiber	n/a	Power mod.	µs	4348	191	200	95.7%	Ti6Al4V	n/a
76	2016	Renishaw AM 250	Fiber	n/a	Power mod.	µs	6410	200	223	89.7%	AlSi10Mg	99.5%
77	2016	Renishaw AM 250	Fiber	70	Power mod.	µs	8771.93	200	228	87.7%	AISI 316L	97.7%

References

1. Concept Laser. http://www.conceptlaserinc.com/machines/

2. EOS e-Manufacturing Solutions. http://www.eos.info/systems_solutions/metal

3. Sisma Additive Manufacturing. http://www.sisma.com/eng/additive-manufacturing/

4. SLM Solutions. http://slm-solutions.com/machines

5. Realizer SLM. http://www.realizer.com/en/startseite/machinery-equipment/machinery-slm50-slm100-slm125-slm250-slm300

6. Renishaw. http://www.renishaw.com/en/additive-manufacturing-systems--15239

7. Kuo TY, Lin YD (2007) Effects of Different Shielding Gases and Power Waveforms on Penetration Characteristics and Porosity Formation in Laser Welding of Inconel 690 Alloy. *Mater. Trans.*, vol. 48, no. 2, pp. 219–226.

8. Demir AG, Pangovski K, O'Neill W, Previtali B (2015) Investigation of pulse shape characteristics on the laser ablation dynamics of TiN coatings in the ns regime. *J. Phys. D. Appl. Phys.*, vol. 48, p. 235202 (11pp).

9. O'Neill W, Sutcliffe C, Morgan R, Hon KKB (1998) Investigation of short pulse Nd: YAG laser interaction with stainless steel powder beds. *Proc. SFF Symp.*.

10. Shiomi M, Yoshidome A, Abe F, Osakada K (1999) Finite element analysis of melting and solidifying processes in laser rapid prototyping of metallic powders. *Int. J. Mach. Tools Manuf.*, vol. 39, no. 2, pp. 237–252.

11. Kathuria YP (1999) Microstructuring by selective laser sintering of metallic powder. *Surf. Coatings Technol.*, vol. 116–119, pp. 643–647.

12. Morgan R, Sutcliffe CJ, O'Neill W (2001) Experimental investigation of nanosecond pulsed Nd:YAG laser re-melted pre-placed powder beds. *Rapid Prototyp. J.*, vol. 7, no. 3, pp. 159–172.

13. Abe F, Osakada K, Shiomi M, Uematsu K, Matsumoto M (2001) The manufacturing of hard tools from metallic powders by selective laser melting. *J. Mater. Process. Technol.*, vol. 111, no. 1–3, pp. 210–213.

14. Edson S, F A, Y K, Osakada K, Shiomi M (2002) Mechanical properties of pure titanium models processed by selective laser melting. in *Proc. of Solid Freeform Fabrication Symposium of Solid*, vol. 1, pp. 180–186.

15. Chatterjee A N, Kumar S, Saha P, Mishra P K, Choudhury A R (2003) An experimental design approach to selective laser sintering of low carbon steel. *J. Mater. Process. Technol.*, vol. 136, no. 1–3, pp. 151–157.

16. Fischer P, Romano V, Weber H P, Karapatis N P, Boillat E, Glardon R (2003) Sintering of commercially pure titanium powder with a Nd:YAG laser source. *Acta Mater.*, vol. 51, no. 6, pp. 1651–1662.

17. Morgan R, Sutcliffe CJ, O'Neill W (2004) Density analysis of direct metal laser re-melted 316L stainless steel cubic primitives. *J. Mater. Sci.*, vol. 39, no. 4, pp. 1195–1205.

18. Regenfuss P, Ebert R, Klötzer S, Hartwig L, Exner H, Brabant T, Petsch T (2004) Industrial laser micro sintering. in *Proceedings of the 4th LANE*, p. 12.

19. Regenfuss P, Hartwig L, Klötzer S, Ebert R, Exner H (2003) Microparts by a Novel Modification of Selective Laser Sintering. *Rapid Prototyp. Manuf. Conf.*, pp. 1–7.

20. Rombouts M, Froyen L, Kruth J, Van Vaerenbergh J (2004) Production and properties of dense iron based parts produced by laser melting with plasma formation. in *Proceedings of the Powder Metallurgy World Congress*, pp. 2–7.

21. Fischer P, Romano V, Weber HP, Kolossov S (2004) Pulsed laser sintering of metallic powders. *Thin Solid Films*, vol. 453–454, pp. 139–144.

22. Kruth JP, Froyen L, Van Vaerenbergh J, Mercelis P, Rombouts M., Lauwers B (2004) Selective laser melting of iron-based powder. *J. Mater. Process. Technol.*, vol. 149, no. 1–3, pp. 616–622.

23. Regenfuss P, Streek A, Hartwig L (2005) Advancements in laser micro sintering. *Proc. Third Int. WLT-Conference Lasers in Manufacturing.* pp. 1–4.

24. Regenfuss P, Hartwig L, Klötzer S, Ebert R, Brabant T, Petsch,, T Exner H (2005) Industrial freeform generation of microtools by laser micro sintering. *Rapid Prototyp. J.*, vol. 11, no. 1, pp. 18–25.

25. Hayashi T, Maekawa K, Tamura M, Hanyu K (2005) Selective Laser Sintering Method Using Titanium Powder Sheet Toward Fabrication of Porous Bone Substitutes. *JSME Int. J. Ser. A*, vol. 48, no. 4, pp. 369–375.

26. Osakada K, Shiomi M (2006) Flexible manufacturing of metallic products by selective laser melting of powder. *Int. J. Mach. Tools Manuf.*, vol. 46, no. 11 SPEC. ISS., pp. 1188–1193.

27. Mumtaz KA, Hopkinson N (2007) Laser melting functionally graded composition of Waspaloy and Zirconia powders. *J. Mater. Sci.*, vol. 42, no. 18, pp. 7647–7656.

28. Regenfuss P, Ebert R, Exner H (2007) Laser Micro Sintering – a Versatile Instrument for the Generation of Microparts. *Laser Tech. J.*, vol. 4, no. 1, pp. 26–31.

29. Regenfuss P, Streek A, Hartwig L, Klötzer S, Brabant T, Horn M, Ebert R, Exner H (2007) Principles of laser micro sintering. *Rapid Prototyp. J.*, vol. 13, no. 4, pp. 204–212.

30. Mumtaz KA, Erasenthiran P, Hopkinson N (2008) High density selective laser melting of Waspaloy®. *J. Mater. Process. Technol.*, vol. 195, no. 1–3, pp. 77–87.

31. Streek A, Regenfuss P, Ebert R (2008) Laser micro sintering–a quality leap through improvement of powder packing. *Proc. 19th Annu. SFF Symp.*, pp. 297–308.

32. Exner H, Horn M, Streek A, Ullmann F, Hartwig L, Regenfuss P, Ebert R (2008) Laser micro sintering: A new method to generate metal and ceramic parts of high resolution with sub-micrometer powder. *Virtual Phys. Prototyp.*, vol. 3, 2014, pp. 3–11.

33. Kruth JP, Yasa E, Deckers J (2008) Roughness improvement in selective laser melting. *Proc. 3rd Int. Conf. Polym. Mould. Innov.*, pp. 170–183.

34. Streek A, Ebert R (2009) Laser micro sintering - Upgrade of the technology. in *Proceedings of ICALEO 2009*, pp. 1–8.

35. Mumtaz K, Hopkinson N (2009) Top surface and side roughness of Inconel 625 parts processed using selective laser melting. *Rapid Prototyp. J.*, vol. 15, no. 2, pp. 96–103.

36. Yasa E, Kruth JP (2010) Investigation of laser and process parameters for Selective Laser Erosion. *Precis. Eng.*, vol. 34, no. 1, pp. 101–112.

37. Mumtaz KA, Hopkinson N (2010) Selective Laser Melting of Inconel 625 Using Pulse Shaping. *Rapid Prototyp. J.*, vol. 16, pp. 165–178.

38. Mumtaz KA, Hopkinson N (2010) Selective Laser Melting of thin wall parts using pulse shaping. *J. Mater. Process. Technol.*, vol. 210, no. 2, pp. 279–287.

39. Ng CC, Savalani M, Man HC (2011) Fabrication of magnesium using selective laser melting technique. *Rapid Prototyp. J.*, vol. 17, no. 6, pp. 479–490.

40. Ng CC, Savalani M, Lau ML, Man HC (2011) Microstructure and mechanical properties of selective laser melted magnesium. *Appl. Surf. Sci.*, vol. 257, no. 17, pp. 7447–7454.

41. Jhabvala J, Boillat E, André C, Glardon R (2012) An innovative method to build support structures with a pulsed laser in the selective laser melting process. *Int. J. Adv. Manuf. Technol.*, vol. 59, no. 1–4, pp. 137–142.

42. Simonelli M, Tse Y, Tuck C (2012) Further understanding of ti-6al-4v selective laser melting using texture analysis. *Solid Free. Fabr. Symp.*, pp. 480–491.

43. Vaithilingam J, Goodridge RD, Christie SD, Edmondson S, Hague RJM (2012) Surface Modification of Selective Laser Melted Structures Using Self-Assembled Monolayers for Biomedical Applications. in *Proc. of Solid Freeform Fabrication Symposium*, no. June.

44. Streek A, Regenfuss P, Exner H (2013) Fundamentals of energy conversion and dissipation in powder layers during laser micro sintering. *Phys. Procedia*, vol. 41, pp. 858–869.

45. Stwora A, Skrabalak G (2013) Influence of selected parameters of Selective Laser Sintering process on properties of sintered materials. *J. Achiev. Mater. Manuf. Eingineering*, vol. 61, no. 2, pp. 375–380.

46. Król M, Dobrzański L, and Reimann I (2013) Surface quality in selective laser melting of metal powders. *Arch. Mater. Sci.*, vol. 60, no. 2, pp. 87–92.

47. Simonelli M, Tse Y, Tuck C (2014) Effect of the build orientation on the mechanical properties and fracture modes of SLM Ti-6Al-4V. *Mater. Sci. Eng. A*, vol. 616, pp. 1–11.

48. Edwards P, Ramulu M (2014) Fatigue performance evaluation of selective laser melted Ti-6Al-4V. *Mater. Sci. Eng. A*, vol. 598, pp. 327–337.

49. Vaithilingam J, Kilsby S, Goodridge RD, Christie SDR, Edmondson S, Hague RJM (2014) Immobilisation of an antibacterial drug to Ti6Al4V components fabricated using selective laser melting. *Appl. Surf. Sci.*, vol. 314, pp. 642–654.

50. Streek A, Exner H (2014) Laser micro melting, in *Proc. of ICALEO*, pp. 895–900.

51. Alrbaey K, Wimpenny D, Tosi R, Manning W, Moroz A (2014) On optimization of surface roughness of selective laser melted stainless steel parts: A statistical study. *J. Mater. Eng. Perform.*, vol. 23, no. 6, pp. 2139–2148.

52. Simonelli M, Tse Y, Tuck C (2014) On the texture formation of selective laser melted Ti-6Al-4V. *Metall. Mater. Trans. A Phys. Metall. Mater. Sci.*, vol. 45, no. 6, pp. 2863–2872.

53. Zhou X, Wang D, Liu X, Zhang D, Qu S, Ma J, London G, Shen Z, Liu W (2015) 3D-imaging of selective laser melting defects in a Co-Cr-Mo alloy by synchrotron radiation micro-CT. *Acta Mater.*, vol. 98, pp. 1–16.

54. Chou R, Milligan J, Paliwal M, Brochu M (2015) Additive Manufacturing of Al-12Si Alloy Via Pulsed Selective Laser Melting. *Jom*, vol. 67, no. 3, pp. 590–596.

55. Vora P, Mumtaz K, Todd I, Hopkinson N (2015) AlSi12 in-situ alloy formation and residual stress reduction using anchorless selective laser melting. *Addit. Manuf.*, vol. 7, pp. 12–19.

56. Zhou X, Liu X, Zhang D, Shen Z, Liu W (2015) Balling phenomena in selective laser melted tungsten. *J. Mater. Process. Technol.*, vol. 222, pp. 33–42.

57. Brown B, Everhart W, Dinardo J (2015) Characterization of Bulk to Thin Wall Mechanical Response Transition in Powder Bed AM. *26th Annu. Int. Solid Free. Fabr. Symp.*, pp. 501–513.

58. Cherry JA, Davies HM, Mehmood S, Lavery NP, Brown SGR, Sienz J (2015) Investigation into the effect of process parameters on microstructural and physical properties of 316L stainless steel parts by selective laser melting. *Int. J. Adv. Manuf. Technol.*, vol. 76, no. 5–8, pp. 869–879.

59. Aboulkhair NT, Stephens A, Maskery I, Tuck C, Ashcroft I, Everitt NM (2015) Mechanical Properties Of Selective Laser Melted AlSi10Mg: Nano, Micro, And Macro Properties. in *Proc. of Solid Freeform Fabrication Symposium*, vol. 1, Intergovernmental Panel on Climate Change, Ed. Cambridge: Cambridge University Press, pp. 1–30.

60. Maskery I, Aremu AO, Simonelli M, Tuck C, Wildman RD, Ashcroft IA, Hague RJM (2015) Mechanical Properties of Ti-6Al-4V Selectively Laser Melted Parts with Body-Centred-Cubic Lattices of Varying cell size. *Exp. Mech.*, pp. 1–12.

61. Aboulkhair NT, Tuck C, Ashcroft IA, Maskery I, Everitt NM (2015) On the Precipitation Hardening of Selective Laser Melted AlSi10Mg. *Metall. Mater. Trans. A Phys. Metall. Mater. Sci.*, vol. 46, no. 8, pp. 3337–3341.

62. Harrison NJ, Todd I, Mumtaz K (2015) Reduction of micro-cracking in nickel superalloys processed by Selective Laser Melting: A fundamental alloy design approach. *Acta Mater.*, vol. 94, pp. 59–68.

63. Davidson K, Singamneni S (2015) Selective Laser Melting of Duplex Stainless Steel Powders; an Investigation. *Mater. Manuf. Process.*, vol. 6914, no. January, p. 150930095558007.

64. Huang Q, Liu X, Yang X, Zhang R, Shen Z, Feng Q (2015) Specific heat treatment of selective laser melted Ti–6Al–4V for biomedical applications. *Front. Mater. Sci.*, vol. 9, no. 4, pp. 373–381.

65. Zhou X, Li K, Zhang D, Liu X, Ma J, Liu W, Shen Z (2015) Textures formed in a CoCrMo alloy by selective laser melting. *J. Alloys Compd.*, vol. 631, pp. 153–164.

66. Bagheri ZS, Melancon D, Liu L, Johnston RB, Pasini D (2016) Compensation strategy to reduce geometry and mechanics mismatches in porous biomaterials built with Selective Laser Melting. *J. Mech. Behav. Biomed. Mater.*, pp. 1–11.

67. Alrbaey K, Wimpenny DI, Al-Barzinjy AA, Moroz A (2016) Electropolishing of Re-melted SLM Stainless Steel 316L Parts Using Deep Eutectic Solvents: 3×3 Full Factorial Design. *J. Mater. Eng. Perform.*.

68. Bai S, Liu J, Yang P, Zhai M, Huang H (2016) Femtosecond Fiber Laser Additive Manufacturing of Tungsten. in *SPIE LASE*, vol. 1, no. 408, pp. 97380U–1–97380U–10.

69. Aboulkhair NT, Maskery I, Tuck C, Ashcroft I, Everitt NM (2016) The microstructure and mechanical properties of selectively laser melted AlSi10Mg: the effect of a conventional T6-like heat treatment. *Mater. Sci. Eng. A*, vol. 104, pp. 174–182.

70. Zhong Y, Liu L, Wikman S, Cui D, Shen Z (2016) Intragranular cellular segregation network structure strengthening 316L stainless steel prepared by selective laser melting. *J. Nucl. Mater.*, vol. 470, pp. 170–178.

71. Bai S, Yang L, Liu J (2016) Manipulation of microstructure in laser additive manufacturing. *Appl. Phys. A Mater. Sci. Process.*, vol. 122, no. 5, pp. 1–5.

72. Trelewicz JR, Halada GP, Donaldson OK, Manogharan G (2016) Microstructure and Corrosion Resistance of Laser Additively Manufactured 316L Stainless Steel. *Jom*, vol. 68, no. 3, pp. 850–859.

73. Morgan HD, Cherry JA, Jonnalaganna S, Ewing D, Sienz J (2016) Part orientation optimisation for the additive layer manufacture of metal components. *Int. J. Adv. Manuf. Technol.*, pp. 1–9.

74. Smith RJ, Hirsch M, Patel R, Li W, Clare AT, Sharples SD (2016) Spatially resolved acoustic spectroscopy for selective laser melting. *J. Mater. Process. Technol.*, vol. 236, pp. 93–102.

75. Vaithilingam J, Goodridge RD, Hague RJM, Christie SDR, Edmondson S (2016) The effect of laser remelting on the surface chemistry of Ti6al4V components fabricated by selective laser melting. *J. Mater. Process. Technol.*, vol. 232, pp. 1–8.

76. Aboulkhair NT, Maskery I, Tuck C, Ashcroft I, Everitt NM (2016) The microstructure and mechanical properties of selectively laser melted AlSi10Mg: the effect of a conventional T6-like heat treatment. *Mater. Sci. Eng. A*, vol. 104, pp. 174–182.

77. Zhu Y, Zou J, Chen X, Yang H (2016) Tribology of selective laser melting processed parts: Stainless steel 316 L under lubricated conditions. *Wear*, vol. 350–351, pp. 46–55.

78. Yasa E, Kempen K, Kruth J (2010) Microstructure and mechanical properties of Maraging Steel 300 after selective laser melting. *Proc. 21st Int. Solid Free. Fabr. Symp.*, pp. 383–396.

79. Contuzzi N, Campanelli SL, Casavola C, Lamberti L (2013) Manufacturing and characterization of 18Ni marage 300 lattice components by selective laser melting. *Materials (Basel).*, vol. 6, no. 8, pp. 3451–3468.

80. Jägle EA, Choi PP, Van Humbeeck J, Raabe D (2014) Precipitation and austenite reversion behavior of a maraging steel produced by selective laser melting. *J. Mater. Res.*, vol. 29, p. 2072.

81. Casalino G, Campanelli SL, Contuzzi N, Ludovico AD (2015) Experimental investigation and statistical optimisation of the selective laser melting process of a maraging steel. *Opt. Laser Technol.*, vol. 65, pp. 151–158.

List of Figures

Figure 1. Schematic representation of a) temporal and b) spatial disposition of pulses.

Figure 2. Main results of the literature survey on the use of PW in SLM. a) Number of articles published per year. Distribution of different b) pulsation mechanisms and c) system types used.

Figure 3. a) Positioning of STL border with respect to the scanned external border and hatch lines composed of different fusion points. b) Change of beam size as function of focal position f.

Figure 4. Size distribution and SEM image of the 18Ni300 maraging steel powder.

Figure 5. Schematic representation of pulse positions within a scan line and between adjacent scan lines.

Figure 6. Technical drawings of the test geometries (a,b) and photographs of the produced parts (c,d). Prism for density study (a,c) and tower for dimensional error characterization (b,d)

Figure 7. a) Main effects plots part density showing the effect of the statistically significant parameter exposure time (t_{on}). b) Density comparison between different processing strategies (error bars represent standard error).

Figure 8. Optical microscopy and SEM images of the sample cross sections showing pore morphology. Highest (a,c) porosity obtained with t_{on}=70 µs and O_p=13% (P_{avg}=168.4 W); and lowest porosity conditions (b,d) obtained with t_{on}=90 µs and O_p=13% (P_{avg}=174.8 W).

Figure 9. a) Main effects plot for dimensional error showing the effect of the statistically significant parameter exposure time (t). b) Dimensional error comparison between different processing strategies (error bars represent standard error).

List of tables

Table 1. Chemical composition of the maraging steel 18Ni300 powder declared by the producer.

Table 2. Fixed and varied parameters as function of test geometries and response variables

Table 3. Process parameter combinations tested in the study with corresponding pulse temporal and spatial characteristics.

Table 4. ANOVA table for density ($\rho\,(\%)$).

Table 5. ANOVA table for average dimensional error (e_{avg}).